THE FLORIDA STATE UNIVERSITY
COLLEGE OF ARTS AND SCIENCES

# VARIABILITY OF SURFACE WIND CONVERGENCE ESTIMATED FROM ERS-1/2 SCATTEROMETER WINDS OVER THE INDIAN OCEAN

By

SONYA C. KULKARNI

A Thesis submitted to the
Department of Meteorology
in partial fulfillment of the
requirements for the degree of
Master of Science

Degree Awarded:
Summer Semester, 1998

Degree Awarded:
Summer Semester, 1998

likelihood estimator (MLE) is used to determine the most probable direction of the wind given a wind speed and a set of directional aliases. The CMOD-IFR2 model has limitations in areas of sharp wind contrasts due to contamination of the measured backscatter by associated weather or because of the spatial resolution. Some of the problems are removed by an ambiguity removal technique which checks the fit and consistancy of statistical qualities with respect to analyses and estimations of other meteorological fields over a swath [*Quilfen*, 1996].

When compared to moored-buoy estimates of the wind speed and direction at 10 m, the estimation of the wind by the scatterometer has a root mean squared (rms) error of 1.2 $ms^{-1}$ in wind speed and rms error near 15° in direction [*Quilfen*, 1996]. The error in the estimated wind speed and direction increases with lower wind speed; the MLE method for determining wind direction tends to perform poorly at speeds less than 3.5 $ms^{-1}$ [*Quilfen*, 1996]. This estimation error could affect divergence calculations in regions of low wind speeds. Our method for estimating divergence, which will be explained in the following section, minimizes the effect of individual wind vectors on the divergence field in an effort to reduce the effect of isolated erroneous values on the calculations.

For the Arabian Sea, the CMOD-IFR2 gives a more accurate estimate of the winds, when compared to other widely used scatterometer wind inversion models. CMOD-IFR2 scatterometer wind-derived products, such as upper ocean transport, also show considerably better agreement to observations [*Halpern et al.*, 1998].

Several problems exist in the ERS scatterometer wind data set. The obvious problems are tied to problems with the satellite. Satellite maneuvers for recalibration or for changing to a new orbit cycle/height usually interrupt the continuous data coverage of the instruments. In addition, the various orbit cycles of the ERS mission sometimes result in poor spatial coverage.

Other anomalies arise from deficiencies with the inversion model and the instru-

sometimes result in poor spatial coverage.

Other anomalies arise from deficiencies with the inversion model and the instru-

ment itself. Although the scatterometer accurately measures the backscatter, the algorithm sometimes has a problem correctly converting the measurement to the 10 m wind vectors. This problem is especially apparent in areas of low wind speed. This algorithm flags those points where the MLE is below a certain value. The inability of the instrument to detect backscatter accurately at low wind speeds exacerbates this problem [*Ebuchi and Graber*, 1998]. Unfortunately, areas of strong convergence, such as the ITCZ, tend to coincide with areas of low wind speeds. Consequently, certain areas of the tropics, especially some of the areas we use for our analysis, are poorly covered by the scatterometer.

*Ebuchi and Graber* [1998] show that there are other problems with the inversion model. In a two month study of scatterometer-derived winds, the CMOD-IFR2 model tended to have a slight systematic bias in determining the correct direction. The derived directions showed a preference to the directions of the three azimuth angles of backscatter measurement.

For this research, we use five years of ERS-1 and ERS-2 scatterometer data, starting with January 1992. This period incorporates most of the measurement phases of both satellites. January to April 1992 and January to March 1994 are periods of poor spatial coverage due to the satellite orbit, a 3-day repeat orbit cycle. This cycle gives good coverage of the poles; however, coverage in the mid-latitudes and tropics is relatively sparse. In addition, June and July 1996 are ignored in the Empirical Orthogonal Function (EOF) analyses because of substantial missing data from satellite maneuvers.

# 3. METHODOLOGY

We use the divergence theorem (equation 1) to calculate horizontal wind divergence in each swath. Previous works (e.g., *Halpern et al.* [1994*a*]; *Zheng et al.* [1997]) have used a finite differenced formula for calculating divergence of satellite estimated winds. Finite difference methods require the winds to be averaged or gridded the winds. This process could result in winds from different swaths being used in the same divergence calculation. Using finite differencing in each swath is extremely difficult to implement due to missing or flagged cells. Our method is more appropriate for satellite data. The divergence theorem method allows us to take advantage of the high spatial resolution of the wind vectors without averaging over different times; it is also more adaptable to regions with missing and/or flagged data.

The divergence theorem states:

$$\int_S (\mathbf{V} \cdot \hat{\mathbf{n}})\, dl = \int_A (\nabla \cdot \mathbf{V})\, dA \tag{1}$$

where $V$ is the vector wind, $A$ is the surface area over which divergence is calculated, and $\hat{\mathbf{n}}$ is the unit vector normal to the perimeter $S$ enclosing $A$ [*Holton*, 1992]. By assuming that the divergence $(\nabla \cdot V)$ is constant within the area, equation (1) is simplified to solve for the horizontal divergence:

$$\nabla \cdot \mathbf{V} = \frac{\int_S (\mathbf{V} \cdot \hat{\mathbf{n}})\, dl}{\int_A dA} \tag{2}$$

For computations, we use all winds from valid cell locations within a certain range of radii (within 0.7 to 1.0° latitude) to create a polygon (surface $A$) surrounding the

For computations, we use all winds from valid cell locations within a certain range of radii (within 0.7 to 1.0° latitude) to create a polygon (surface $A$) surrounding the point for which we are calculating a divergence. Ideally, the polygon created by these

surrounding cells would be convex, perfectly centered about the calculation point. As previously discussed, this data set has several problems leading to missing/flagged data; therefore, a few rules must be implemented to ensure the quality of the divergence calculation.

In this system, missing divergence values result from too few valid wind vectors surrounding the point or too great a distance between successive points on the polygon. Given that the perfect situation should yield greater than 20 valid points, setting the minimum number of valid vectors surrounding the point to 10 forces a maximum number of missing values. One missing value or row of values will not affect the calculation, but several missing values and rows will lead to a missing divergence value.

By limiting the distance between points, we try to create a polygon that is not too far from centered about the point. This distance is judged by the magnitude of the angle difference between successive clockwise points relative to the center point. If the angle between two adjacent points is greater than 160°, the polygon may be too off-center for the divergence calculation to be representative of the true divergence for the calculation point. Using only those points that qualify allows us to gain more confidence and increased accuracy in the divergence calculations.

We compute divergence for a majority of the ice-free oceans (70° S – 70° N, at all longitudes). Each swath is computed separately to avoid overlap of wind vectors from different times. Resulting divergence estimations are binned into 2° latitude by 2° longitude boxes over our area of concentration (40° S – 40° N, 20° E – 120° E; Figure 1) for each day of the five-year period, 1992-1996.

Despite the relatively good spatial and temporal coverage of the scatterometer, several days of divergence calculations are needed to create a global map. We find that the shortest time interval for meaningful averages is monthly. Therefore, the daily mean fields are averaged into monthly means for 1992-1996 period. Annual

that the shortest time interval for meaningful averages is monthly. Therefore, the daily mean fields are averaged into monthly means for 1992-1996 period. Annual

means and climatological (1992-1996) monthly means are also generated from daily means.

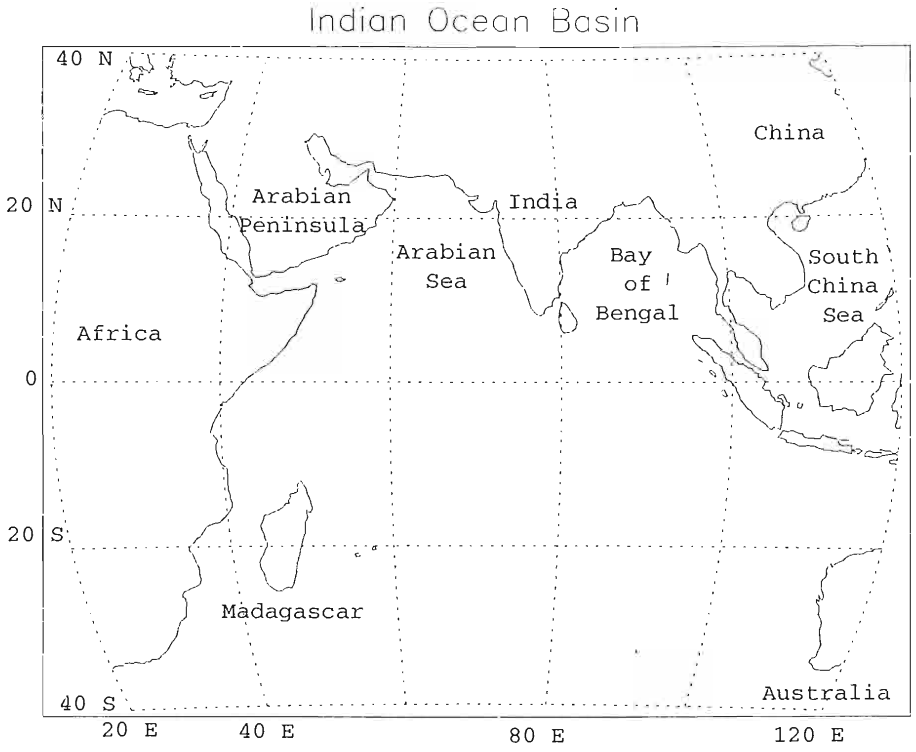


Figure 1: Map of the Indian Ocean Basin. Analysis of results from divergence calculations were carried out over the region from 40° S to 40° N and 20° E to 120° E.

# 4. RESULTS

For consistency, references to seasons in this study are that of the northern hemisphere. Winter includes the months of December, January, February; spring includes March, April, and May; summer incorporates June, July, and August; and fall is considered to be September, October, and November.

## 4.1 Total, annual, and five-year averages

The strongest and most persistent features appear in the five year average of the data (Figure 2). The northern Indian Ocean has net convergence due to the strong convergence experienced with the Asian monsoon in the summer. South of the equator, the ITCZ is the strongest and most persistent feature in this five year period. Over the southwestern part of the Indian Ocean, the convergence is strong throughout the period, while the southeastern ocean ITCZ experiences a strengthening in convergence in during the five year period.

This overall mean compares well with *in situ* studies. For example, the divergence calculated from the FSU Winds data [*Legler et al.*, 1997] shows most of the same features. Locations of the various convergent and divergent zones match up well; however, the divergence and convergence are slightly stronger in our study. Both studies find divergence on the order of $10^{-6}$ $s^{-1}$.

Annually averages of the data reveal the interannual changes during this period (Figure 3). Because the months with less coverage were included for completeness in 1992 and 1994 (Figures 3a and 3c), those annual averages tend to show a band struc-

(Figure 3). Because the months with less coverage were included for completeness in 1992 and 1994 (Figures 3a and 3c), those annual averages tend to show a band structure from the satellite tracks during that period. These averages are also weighted

more toward summer and fall patterns, since the first three to four months have considerably fewer points than other months.

The ITCZ over the southwestern Indian Ocean is strong in 1992 and 1993, with magnitudes exceeding $-1 \times 10^{-5}$ $s^{-1}$ occurring between 5° S and 15° S (Figures 3a and 3b). The eastern section is much weaker and almost non-existent (small patches with minimum values between $-4$ and $-6 \times 10^{-6}$ $s^{-1}$). This part of the ITCZ is also narrower and centered close to 5° S.

During 1994 and 1995 (Figures 3c and 3d), the western part of the ITCZ is still strong. The eastern section, centered now between 5° S and 15° S, is considerably stronger and wider than the earlier years.

In 1996 (Figure 3e), the ITCZ is continuous across the basin; however, it is centered a few degrees further south (13° S) than during 1994 and 1995. Also, it is weaker than the ITCZ in 1995, especially at the eastern and western boundaries.

The convergence and divergence patterns over the southeastern Indian Ocean undergoes a dramatic change in the nature of the divergence between 1993 and 1994 (Figures 3b and 3c, respectively). The region of divergence centered around 20° S disappears. At the same time, the convergence zone centered at 10° S strengthens. The strengthened convergence zone dominates the southeast ocean for the last three years of the period (Figures 3c, 3d, and 3e). This change will be explored further in section 4.4.

The seasonal cycle is emphasized in the monthly climatologies for 1992-1996 (Figures 4, 5, 6, and 7). During the winter (Figure 4), the northern Indian Ocean and regions southwest and west of Australia are generally divergent, while strong convergence is evident between 10° S and 20° S. During January and February, the ITCZ over the southwest Indian Ocean is centered about 20° S near Madagascar. Over the central and eastern Indian Ocean, the ITCZ is farther north, between 5° S and 15° S.

In spring (Figure 5), the divergence over the northern ocean shifts to the eastern central and eastern Indian Ocean, the ITCZ is farther north, between 5° S and 15° S.

In spring (Figure 5), the divergence over the northern ocean shifts to the eastern

part of the Arabian Sea and Bay of Bengal as the beginning of the transition to the summer pattern in the Indian Ocean. Another part of this seasonal transition occurs in the ITCZ. West of 70° E, the ITCZ begins to migrate northward. Some convergence even begins to appear north of the equator near 70° E. The entire ITCZ is slightly weaker during spring than the winter months due to the changing cross-equatorial wind flow.

With the onset of the Asian monsoon in late spring and early summer (Figures 5c and 6), patterns over the Arabian Sea and Bay of Bengal exhibit strong convergence (stronger than $-15 \times 10^{-6}$ $s^{-1}$) except in the region of the Somali Jet (50° E, 0°to 10° N). The acceleration of the winds in this area results in strong divergence. Over the southwest Indian Ocean, the convergence is relatively strong, but it is located farther north (5° S to 10° S) than the winter convergence zone (close to 20° S). The convergence is weaker over the southeast Indian Ocean, but the zone is still in the same general location as the winter months (5° S to 15° S). Some convergence still exists north of the equator near 70° E.

In the fall (Figure 7), the divergence patterns begin to revert back to the winter configuration. The ITCZ is relatively weak, and the western section is slowly propagating to the south. The convergent features north of the equator at 70° E begin to dissipate. The convergence over the northern part of the ocean weakens and begins to disappear as winter approaches.

This seasonal cycle is similar to the seasonal cycle of divergence noted in other studies. The strength and location of the ITCZ in the southwestern Indian Ocean compares well to a study by *Jury et al.* [1994]. A study of highly reflective cloud (HRC) data shows some of the same convergent features of the eastern part of the basin [*Waliser and Gautier*, 1993]. In addition, the behavior of the surface winds and wind divergence over the northern ocean is also documented; our study compares well to these studies (e.g., *Hastenrath* [1991]; *Legler et al.* [1997]). However, these studies

wind divergence over the northern ocean is also documented; our study compares well to these studies (e.g., *Hastenrath* [1991]; *Legler et al.* [1997]). However, these studies

likelihood estimator (MLE) is used to determine the most probable direction of the wind given a wind speed and a set of directional aliases. The CMOD-IFR2 model has limitations in areas of sharp wind contrasts due to contamination of the measured backscatter by associated weather or because of the spatial resolution. Some of the problems are removed by an ambiguity removal technique which checks the fit and consistancy of statistical qualities with respect to analyses and estimations of other meteorological fields over a swath [*Quilfen*, 1996].

When compared to moored-buoy estimates of the wind speed and direction at 10 m, the estimation of the wind by the scatterometer has a root mean squared (rms) error of 1.2 $ms^{-1}$ in wind speed and rms error near 15° in direction [*Quilfen*, 1996]. The error in the estimated wind speed and direction increases with lower wind speed; the MLE method for determining wind direction tends to perform poorly at speeds less than 3.5 $ms^{-1}$ [*Quilfen*, 1996]. This estimation error could affect divergence calculations in regions of low wind speeds. Our method for estimating divergence, which will be explained in the following section, minimizes the effect of individual wind vectors on the divergence field in an effort to reduce the effect of isolated erroneous values on the calculations.

For the Arabian Sea, the CMOD-IFR2 gives a more accurate estimate of the winds, when compared to other widely used scatterometer wind inversion models. CMOD-IFR2 scatterometer wind-derived products, such as upper ocean transport, also show considerably better agreement to observations [*Halpern et al.*, 1998].

Several problems exist in the ERS scatterometer wind data set. The obvious problems are tied to problems with the satellite. Satellite maneuvers for recalibration or for changing to a new orbit cycle/height usually interrupt the continuous data coverage of the instruments. In addition, the various orbit cycles of the ERS mission sometimes result in poor spatial coverage.

Other anomalies arise from deficiencies with the inversion model and the instru-

sometimes result in poor spatial coverage.

Other anomalies arise from deficiencies with the inversion model and the instru-

ment itself. Although the scatterometer accurately measures the backscatter, the algorithm sometimes has a problem correctly converting the measurement to the 10 m wind vectors. This problem is especially apparent in areas of low wind speed. This algorithm flags those points where the MLE is below a certain value. The inability of the instrument to detect backscatter accurately at low wind speeds exacerbates this problem [*Ebuchi and Graber*, 1998]. Unfortunately, areas of strong convergence, such as the ITCZ, tend to coincide with areas of low wind speeds. Consequently, certain areas of the tropics, especially some of the areas we use for our analysis, are poorly covered by the scatterometer.

*Ebuchi and Graber* [1998] show that there are other problems with the inversion model. In a two month study of scatterometer-derived winds, the CMOD-IFR2 model tended to have a slight systematic bias in determining the correct direction. The derived directions showed a preference to the directions of the three azimuth angles of backscatter measurement.

For this research, we use five years of ERS-1 and ERS-2 scatterometer data, starting with January 1992. This period incorporates most of the measurement phases of both satellites. January to April 1992 and January to March 1994 are periods of poor spatial coverage due to the satellite orbit, a 3-day repeat orbit cycle. This cycle gives good coverage of the poles; however, coverage in the mid-latitudes and tropics is relatively sparse. In addition, June and July 1996 are ignored in the Empirical Orthogonal Function (EOF) analyses because of substantial missing data from satellite maneuvers.

# 3. METHODOLOGY

We use the divergence theorem (equation 1) to calculate horizontal wind divergence in each swath. Previous works (e.g., *Halpern et al.* [1994*a*]; *Zheng et al.* [1997]) have used a finite differenced formula for calculating divergence of satellite estimated winds. Finite difference methods require the winds to be averaged or gridded the winds. This process could result in winds from different swaths being used in the same divergence calculation. Using finite differencing in each swath is extremely difficult to implement due to missing or flagged cells. Our method is more appropriate for satellite data. The divergence theorem method allows us to take advantage of the high spatial resolution of the wind vectors without averaging over different times; it is also more adaptable to regions with missing and/or flagged data.

The divergence theorem states:

$$\int_S (\mathbf{V} \cdot \hat{\mathbf{n}})\, dl = \int_A (\nabla \cdot \mathbf{V})\, dA \tag{1}$$

where $V$ is the vector wind, $A$ is the surface area over which divergence is calculated, and $\hat{\mathbf{n}}$ is the unit vector normal to the perimeter $S$ enclosing $A$ [*Holton*, 1992]. By assuming that the divergence $(\nabla \cdot V)$ is constant within the area, equation (1) is simplified to solve for the horizontal divergence:

$$\nabla \cdot \mathbf{V} = \frac{\int_S (\mathbf{V} \cdot \hat{\mathbf{n}})\, dl}{\int_A dA} \tag{2}$$

For computations, we use all winds from valid cell locations within a certain range of radii (within 0.7 to 1.0° latitude) to create a polygon (surface $A$) surrounding the

For computations, we use all winds from valid cell locations within a certain range of radii (within 0.7 to 1.0° latitude) to create a polygon (surface $A$) surrounding the point for which we are calculating a divergence. Ideally, the polygon created by these

surrounding cells would be convex, perfectly centered about the calculation point. As previously discussed, this data set has several problems leading to missing/flagged data; therefore, a few rules must be implemented to ensure the quality of the divergence calculation.

In this system, missing divergence values result from too few valid wind vectors surrounding the point or too great a distance between successive points on the polygon. Given that the perfect situation should yield greater than 20 valid points, setting the minimum number of valid vectors surrounding the point to 10 forces a maximum number of missing values. One missing value or row of values will not affect the calculation, but several missing values and rows will lead to a missing divergence value.

By limiting the distance between points, we try to create a polygon that is not too far from centered about the point. This distance is judged by the magnitude of the angle difference between successive clockwise points relative to the center point. If the angle between two adjacent points is greater than 160°, the polygon may be too off-center for the divergence calculation to be representative of the true divergence for the calculation point. Using only those points that qualify allows us to gain more confidence and increased accuracy in the divergence calculations.

We compute divergence for a majority of the ice-free oceans (70° S – 70° N, at all longitudes). Each swath is computed separately to avoid overlap of wind vectors from different times. Resulting divergence estimations are binned into 2° latitude by 2° longitude boxes over our area of concentration (40° S – 40° N, 20° E – 120° E; Figure 1) for each day of the five-year period, 1992-1996.

Despite the relatively good spatial and temporal coverage of the scatterometer, several days of divergence calculations are needed to create a global map. We find that the shortest time interval for meaningful averages is monthly. Therefore, the daily mean fields are averaged into monthly means for 1992-1996 period. Annual

that the shortest time interval for meaningful averages is monthly. Therefore, the daily mean fields are averaged into monthly means for 1992-1996 period. Annual

means and climatological (1992-1996) monthly means are also generated from daily means.

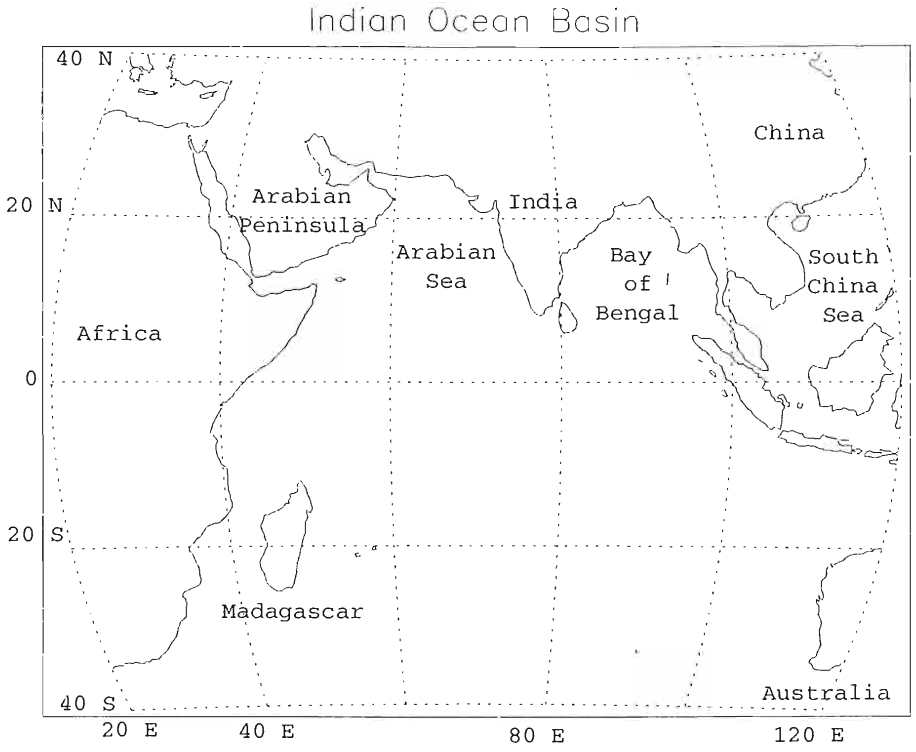


Figure 1: Map of the Indian Ocean Basin. Analysis of results from divergence calculations were carried out over the region from 40° S to 40° N and 20° E to 120° E.

# 4. RESULTS

For consistency, references to seasons in this study are that of the northern hemisphere. Winter includes the months of December, January, February; spring includes March, April, and May; summer incorporates June, July, and August; and fall is considered to be September, October, and November.

## 4.1 Total, annual, and five-year averages

The strongest and most persistent features appear in the five year average of the data (Figure 2). The northern Indian Ocean has net convergence due to the strong convergence experienced with the Asian monsoon in the summer. South of the equator, the ITCZ is the strongest and most persistent feature in this five year period. Over the southwestern part of the Indian Ocean, the convergence is strong throughout the period, while the southeastern ocean ITCZ experiences a strengthening in convergence in during the five year period.

This overall mean compares well with *in situ* studies. For example, the divergence calculated from the FSU Winds data [*Legler et al.*, 1997] shows most of the same features. Locations of the various convergent and divergent zones match up well; however, the divergence and convergence are slightly stronger in our study. Both studies find divergence on the order of $10^{-6}$ $s^{-1}$.

Annually averages of the data reveal the interannual changes during this period (Figure 3). Because the months with less coverage were included for completeness in 1992 and 1994 (Figures 3a and 3c), those annual averages tend to show a band struc-

(Figure 3). Because the months with less coverage were included for completeness in 1992 and 1994 (Figures 3a and 3c), those annual averages tend to show a band structure from the satellite tracks during that period. These averages are also weighted

more toward summer and fall patterns, since the first three to four months have considerably fewer points than other months.

The ITCZ over the southwestern Indian Ocean is strong in 1992 and 1993, with magnitudes exceeding $-1 \times 10^{-5}$ $s^{-1}$ occurring between 5° S and 15° S (Figures 3a and 3b). The eastern section is much weaker and almost non-existent (small patches with minimum values between $-4$ and $-6 \times 10^{-6}$ $s^{-1}$). This part of the ITCZ is also narrower and centered close to 5° S.

During 1994 and 1995 (Figures 3c and 3d), the western part of the ITCZ is still strong. The eastern section, centered now between 5° S and 15° S, is considerably stronger and wider than the earlier years.

In 1996 (Figure 3e), the ITCZ is continuous across the basin; however, it is centered a few degrees further south (13° S) than during 1994 and 1995. Also, it is weaker than the ITCZ in 1995, especially at the eastern and western boundaries.

The convergence and divergence patterns over the southeastern Indian Ocean undergoes a dramatic change in the nature of the divergence between 1993 and 1994 (Figures 3b and 3c, respectively). The region of divergence centered around 20° S disappears. At the same time, the convergence zone centered at 10° S strengthens. The strengthened convergence zone dominates the southeast ocean for the last three years of the period (Figures 3c, 3d, and 3e). This change will be explored further in section 4.4.

The seasonal cycle is emphasized in the monthly climatologies for 1992-1996 (Figures 4, 5, 6, and 7). During the winter (Figure 4), the northern Indian Ocean and regions southwest and west of Australia are generally divergent, while strong convergence is evident between 10° S and 20° S. During January and February, the ITCZ over the southwest Indian Ocean is centered about 20° S near Madagascar. Over the central and eastern Indian Ocean, the ITCZ is farther north, between 5° S and 15° S.

In spring (Figure 5), the divergence over the northern ocean shifts to the eastern central and eastern Indian Ocean, the ITCZ is farther north, between 5° S and 15° S.

In spring (Figure 5), the divergence over the northern ocean shifts to the eastern

part of the Arabian Sea and Bay of Bengal as the beginning of the transition to the summer pattern in the Indian Ocean. Another part of this seasonal transition occurs in the ITCZ. West of 70° E, the ITCZ begins to migrate northward. Some convergence even begins to appear north of the equator near 70° E. The entire ITCZ is slightly weaker during spring than the winter months due to the changing cross-equatorial wind flow.

With the onset of the Asian monsoon in late spring and early summer (Figures 5c and 6), patterns over the Arabian Sea and Bay of Bengal exhibit strong convergence (stronger than $-15 \times 10^{-6}$ $s^{-1}$) except in the region of the Somali Jet (50° E, 0°to 10° N). The acceleration of the winds in this area results in strong divergence. Over the southwest Indian Ocean, the convergence is relatively strong, but it is located farther north (5° S to 10° S) than the winter convergence zone (close to 20° S). The convergence is weaker over the southeast Indian Ocean, but the zone is still in the same general location as the winter months (5° S to 15° S). Some convergence still exists north of the equator near 70° E.

In the fall (Figure 7), the divergence patterns begin to revert back to the winter configuration. The ITCZ is relatively weak, and the western section is slowly propagating to the south. The convergent features north of the equator at 70° E begin to dissipate. The convergence over the northern part of the ocean weakens and begins to disappear as winter approaches.

This seasonal cycle is similar to the seasonal cycle of divergence noted in other studies. The strength and location of the ITCZ in the southwestern Indian Ocean compares well to a study by *Jury et al.* [1994]. A study of highly reflective cloud (HRC) data shows some of the same convergent features of the eastern part of the basin [*Waliser and Gautier*, 1993]. In addition, the behavior of the surface winds and wind divergence over the northern ocean is also documented; our study compares well to these studies (e.g., *Hastenrath* [1991]; *Legler et al.* [1997]). However, these studies

wind divergence over the northern ocean is also documented; our study compares well to these studies (e.g., *Hastenrath* [1991]; *Legler et al.* [1997]). However, these studies

are limited by the lack of *in situ* wind data available in the Indian Ocean, especially the southern ocean. The scatterometer helps identify climatological features in this area.

### 4.2 Variations in time at a meridian

A strong seasonality over the Arabian sea (60° E) and the Bay of Bengal (90° E) is evident from the changes in divergence patterns through the period (Figure 8). This seasonality reflects the seasonal nature of the Asian monsoon flow. Maximum values of convergence (exceeding $-4 \times 10^{-5}$ s$^{-1}$ are found in the summer monsoon months, and strong divergence occurs during the winter months.

South of the equator at 60° E (Figure 8a), seasonality still exists in the ITCZ, but this seasonal cycle is much less pronounced than over the Arabian Sea. During December, January, and February, the ITCZ tends to be centered at 13° S. In the spring, the ITCZ propagates slightly northward to roughly 10° S. The ITCZ remains at this position until September, the beginning of the transition back to the winter pattern.

During the transitions between the summer and winter positions (Figure 8a), the ITCZ tends to be slightly weaker with minimum values generally between $-1$ and $-2 \times 10^{-5}$ s$^{-1}$. At the seasonal extremes (winter and summer), the ITCZ is generally stronger with convergence exceeding $-4 \times 10^{-5}$ s$^{-1}$. The summer convergence is mainly due to a bend in the trade winds into the monsoon flow near the equator, while the winter band emerges from the confluence of the southern trade winds and the northerly flow from the Arabian Sea. During both of these times, the convergence is fairly strong, but the transition between the two regimes leads to a weakening of the convergence in spring and fall.

At 90° E (Figure 8b), the divergence patterns change dramatically in 1994 between 30° S and the equator. The strong divergence zone between 15° S and 30° S weakens

At 90° E (Figure 8b), the divergence patterns change dramatically in 1994 between 30° S and the equator. The strong divergence zone between 15° S and 30° S weakens considerably, while the convergence zone between 15° S and the equator strengthens

and is consistently strong. The strongest convergence values are in 1994; however, areas of convergence with magnitudes greater than $-2 \times 10^{-5}\ s^{-1}$ still appear in 1995 and 1996. Further discussion of this change in divergence patterns can be found later (section 4.4).

### 4.3 Empirical Orthogonal Function analysis

We use empirical orthogonal functions (EOF) to find the major contributions to the variations within the period. Very briefly, a data set can be described as a sum of orthogonal components:

$$\boldsymbol{D_{s,t}} = \sum_i a_{i,t} X_{i,s};\ s = 1, \ldots, S,\ t = 1, \ldots, T \tag{3}$$

where $D(s,t)$ is the data point at location $s$ and time $t$, $a$ is the temporal variation of the $i^{th}$ component, and $X$ is the spatial pattern of the $i^{th}$ component. EOF analysis breaks up the spatial and temporal variance of the data set into a number ($i$) of separate space and time components. Individual components can be ranked according to the amount of the total variance explained. One expects the first several EOFs to explain a majority of the variance [*Wilks*, 1995; *Legler*, 1983]. This variance includes seasonal variations, since we do not remove the seasonal means prior to analysis. In addition, this analysis requires no missing data; therefore, the nine months with missing data are excluded.

Using a scree test [*Wilks*, 1995], we determine that the first four EOFs are the only EOFs that are statistically significant. The first EOF comprises 15.9% of the explained variance, while the second, third, and fourth EOFs represent 5.4%, 3.8%, and 3.4% over the variance, respectively.

The first EOF emphasizes part of the annual cycle (Figure 9). The most striking features in the spatial pattern are several regions of convergence. The Arabian Sea, Bay of Bengal, the area just south of India, ITCZ, and a narrow band near 40° S all features in the spatial pattern are several regions of convergence. The Arabian Sea, Bay of Bengal, the area just south of India, ITCZ, and a narrow band near 40° S all have large areas of convergence. Several divergent features are also evident off the

coast of Somalia, west of Madagascar and west of Australia. The temporal component shows that the spatial features found in EOF 1 are summer features over the Indian Ocean. We note that the last three years of the associated time series have a slightly higher maximum during the summer months than 1992 and 1993.

The second EOF also shows elements of the annual cycle (Figure 10); however it has a much stronger interannual component than EOF 1. The major features in the spatial pattern are strong convergent areas over the Arabian Sea, Bay of Bengal, and north of Madagascar and a strong divergent patch over the southeastern Indian Ocean (70° E to 120° E, centered about 10° S). For 1992 and 1993, the summer features are more pronounced: convergence in the northern ocean, convergence north of Madagascar, and divergence in the southeast Indian Ocean. For 1994 to 1996, the winter features are dominant. The Arabian Sea and Bay of Bengal are divergent, and there is strong convergence centered about 10° S. The area north of Madagascar is also divergent; this feature, along with a similar feature in EOF 1, emphasizes the seasonal migration of the ITCZ in the western ocean. The interannual trend seen in EOF 2 attaches a statistical significance to the change in 1994.

The third and fourth EOFs clearly expose the shift in 1994 in the nature of the divergence in the southeast Indian Ocean (Figures 11 and 12). The region where the changes occur is depicted in both EOFs.

The region from 10° S to 30° S and east of 70° E is emphasized in EOF 3 (Figure 11). By examining the temporal component, divergence is evident in the region for the first two years of the period. At the beginning of 1994, this shifts dramatically to convergence. Convergence persists in the region until later 1996.

The entire band centered at 10° S is highlighted in the spatial function of EOF 4 (Figure 12); however, the eastern half is mainly convergent while the western part is more divergent. The temporal component shows that this contrast is the main pattern for 1992 and 1993. The eastern half of the area is divergent while the western is more divergent. The temporal component shows that this contrast is the main pattern for 1992 and 1993. The eastern half of the area is divergent while the western

half is convergent. Very little can be inferred from the latter portion of the period with the exception of a large spike in mid-1996. This spike corresponds to larger convergence values over the southeastern Indian Ocean.

### 4.4 Changes over the southeast Indian Ocean

As previously discussed, between late 1993 and early 1994, the divergence patterns change over the southeast Indian Ocean. This shift in the nature of the divergence in this region arises in several analyses of the calculated field (Figures 8b, 3b and 3c, and 11 and 12). Analyses of other related fields help offer an explanation for this change.

In order to diagnose any changes in the nature of the southeast trade winds, we use an index of the trade wind anomalies. These anomalies are the differences in wind strength from the seasonal means. Our southeast trade wind index is calculated from the monthly FSU wind field [*Stricherz et al.*, 1993; *Legler et al.*, 1997] by averaging the magnitude of the monthly FSU wind anomalies. The index box, 75° E to 95° E and 17° S to 20° S, incorporates the core of the southeast trade winds. The resulting index shows the month to month changes in the trade wind anomalies (Figure 13).

Starting in January 1994, the index indicates a change in wind strength. Prior to 1994, the trade winds are on the average weaker than the wind of the latter years of the period. A standard Student's t-test is used to determine whether the difference in the mean trade wind strength between 1992-1993 and 1994-1996 is statisticlly significant [*Wilks*, 1995]. Results from the t-test show that the increase in mean trade wind strength between 1992-1993 and 1994-1996 is significant (t-test value of 0.00695).

Strengthening of the southeast trade winds in the index box results in greater convergence north of 17° S and decreased divergence to the south. Convergence north of this latitude is strong starting in 1994. The strong divergence south of 17° S during 1992 and 1993 weakens and virtually disappears for the latter part of the north of this latitude is strong starting in 1994. The strong divergence south of 17° S during 1992 and 1993 weakens and virtually disappears for the latter part of the period.

The change in the surface wind divergence between 10° S and 20° S along with the associated change in trade winds is also reflected in other fields. Sea surface temperature (SST) may be related to surface wind divergence. Several studies have noted a relationship between SST and tropical convergence (e.g., *Hastenrath and Lamb* [1978]; *Jury and Pathack* [1991]). Although it is still unclear whether the location of the ITCZ affects the underlying SST values or vice versa, it is evident that higher SSTs tend to be collocated with the ITCZ [*Hastenrath and Lamb*, 1978]. Over the southeast Indian Ocean, the SST patterns can also be affected by the Indonesian throughflow [*Reason et al.*, 1996; *Meyers*, 1996] and wind-induced upwelling off the coast of Sumatra [*Meyers*, 1996].

Using monthly Reynolds SST data [*Reynolds and Smith*, 1994], we note several interesting features. The increase in wind strength may lead to a slight drop in SST anomalies (from seasonal means) between 5° S and 15° S (Figures 14 and 15). This decrease in SST is part of a cold event previously identified by *Meyers* [1996] as wind-induced coastal upwelling combined with possible El Niño effects via the Indonesian throughflow.

Starting at the end of 1994, the SSTs start increasing between 10° S and 20° S (Figures 15a and 16a) and return to higher anomalies north of 10° S; this pattern may be in response to the stronger convergence zone. Higher SSTs favor the location of the tropical convergence (Figures 15c and 16c).

Areas of surface wind convergence in the tropics are characterized by convective cloud activity. OLR tends to be a useful tool for measuring convective cloud cover; Lower values of OLR indicate more convective cloud activity and can indicate changes in the ITCZ [*Waliser and Gautier*, 1993]. However, cloud activity and OLR are also sensitive to changes in SST; cold anomalies in SST often lead to less sustained convective cloud activity and higher values of OLR.

The OLR field tends to mirror the changes in SST between 5° S and 15° S (Fig-
convective cloud activity and higher values of OLR.

The OLR field tends to mirror the changes in SST between 5° S and 15° S (Fig-

ures 15 and 14). Smaller anomalies in SST lead to greater anomalies in OLR. In the southeast Indian Ocean, the increase in trade wind strength and associated drop in SST lead to large OLR anomalies. The effect of the convergence may bring about the return to negative anomalies, indicating more convective cloud activity. South of 15° S, the mean SST values (less than 25°C) are too cold to support sustained convective cloud activity. Any cloud activity is relatively short-lived and does not appear to be significant to the monthly mean OLR field. Therefore, OLR shows little change despite changes in both the SST and divergence fields (Figure 16).

It is important to note that the change in divergence patterns in 1994 is not clearly evident in other studies of the atmospheric circulation in the southeast Indian Ocean (e.g., *Legler et al.* [1997]). However, most of these studies rely on assimilated ship and buoy data, and southern ocean tends to be poorly sampled by these sources.

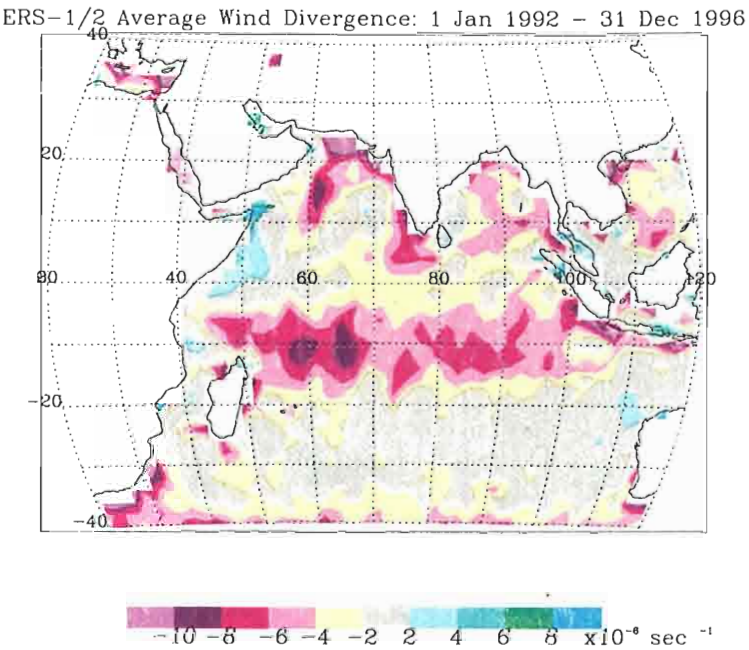


Figure 2: Average wind divergence from ERS-1/2 scatterometer data for all five years of study. Convergence is shown as negative divergence. Units are $10^{-6}$ $s^{-1}$.

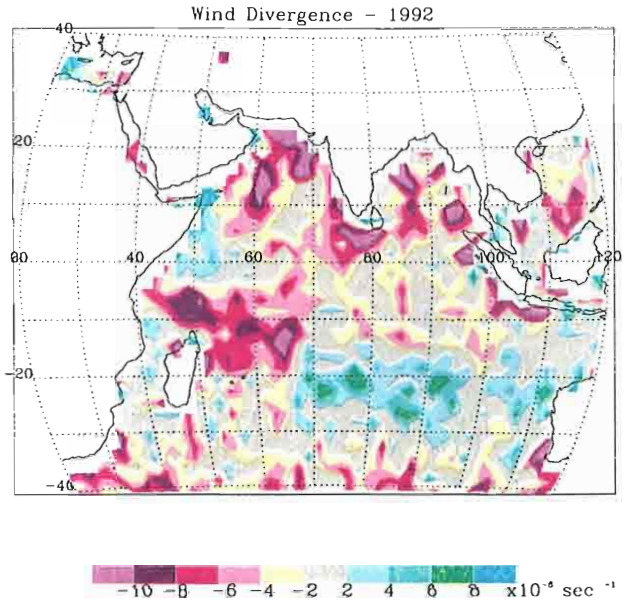


(a) 1992

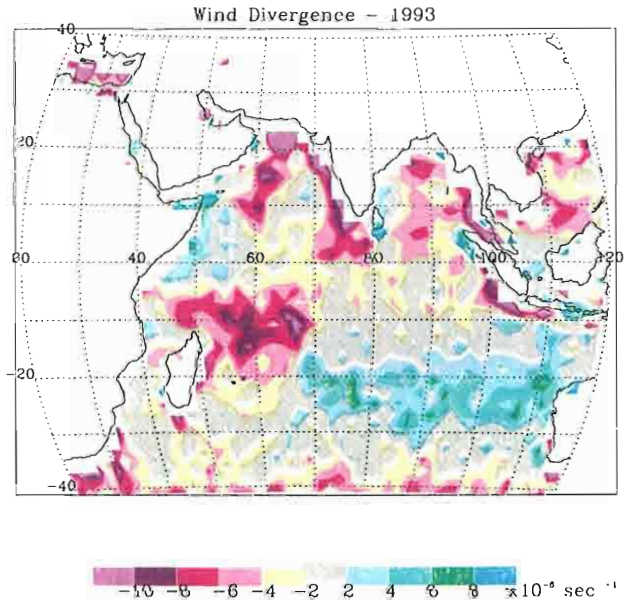


(b) 1993

Figure 3: Annually averaged wind divergence for 1992 through 1996. Convergence is shown as negative divergence. Units are $10^{-6}$ $s^{-1}$.

Figure 3: Annually averaged wind divergence for 1992 through 1996. Convergence is shown as negative divergence. Units are $10^{-6}$ $s^{-1}$.

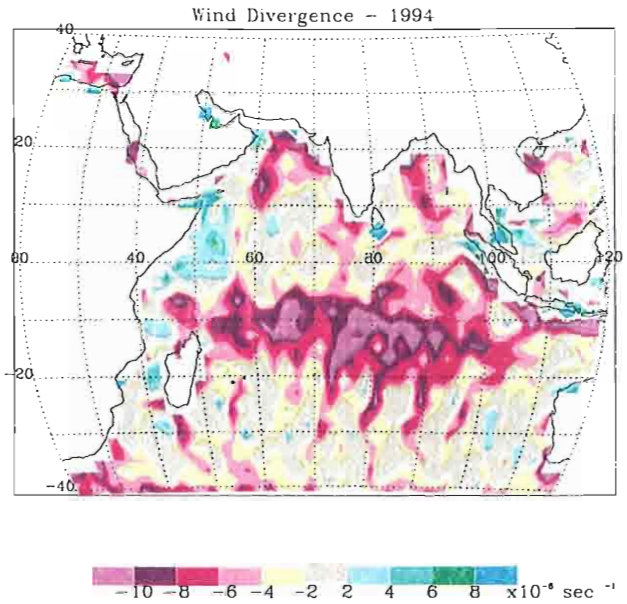


(c) 1994

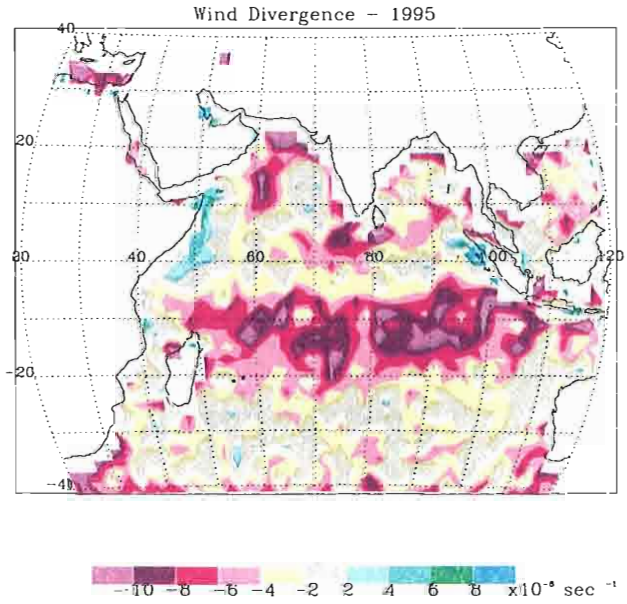


(d) 1995

Figure 3: continued.

Figure 3: continued.

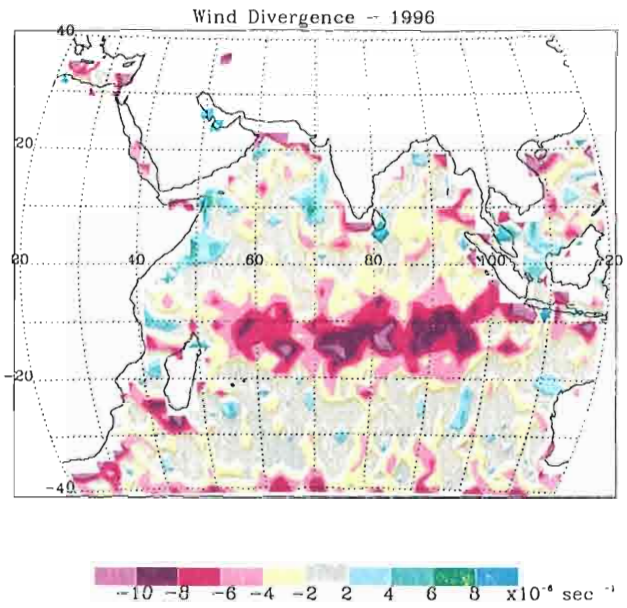


(e) 1996

Figure 3: continued

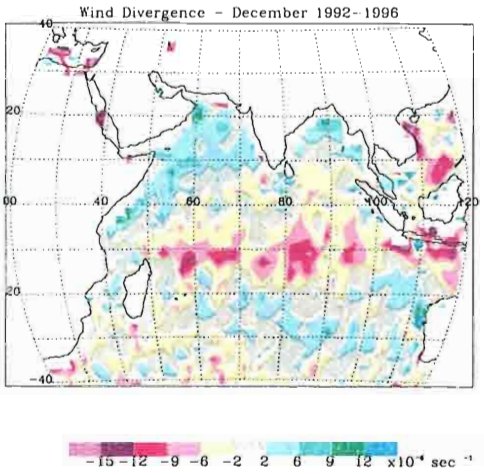


(a) December

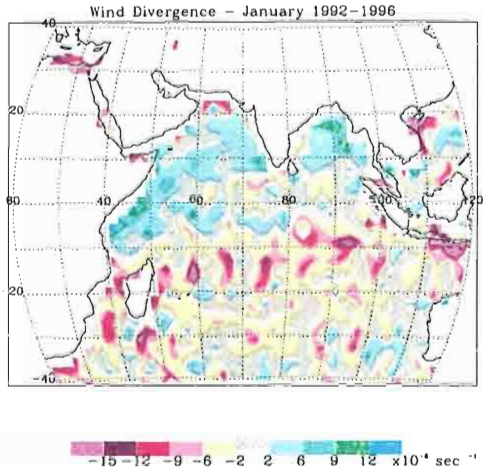


(b) January

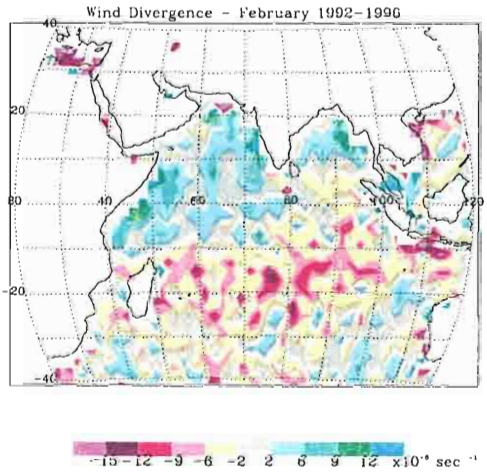


(c) February

Figure 4: Climatological (1992-1996) divergence for December, January, and February averaged over all five years. Convergence is shown as negative divergence. Units are $10^{-6}$ $s^{-1}$.

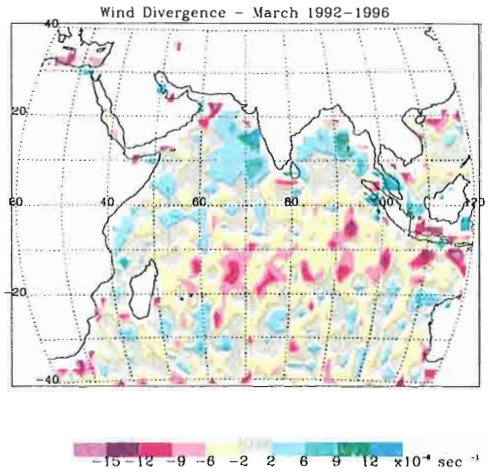


(a) March

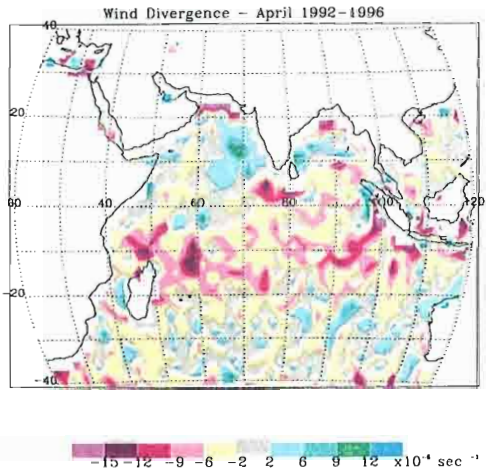


(b) April

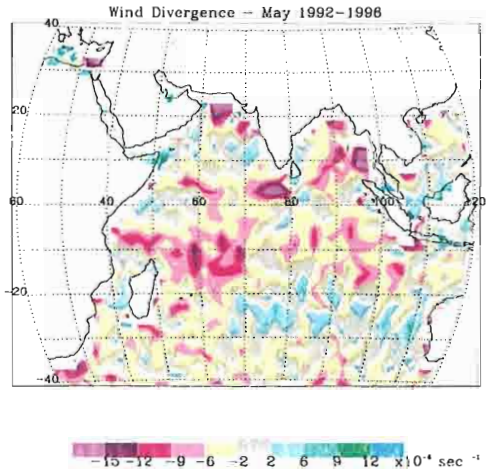


(c) May

Figure 5: Same as figure 4 except for March, April, and May.

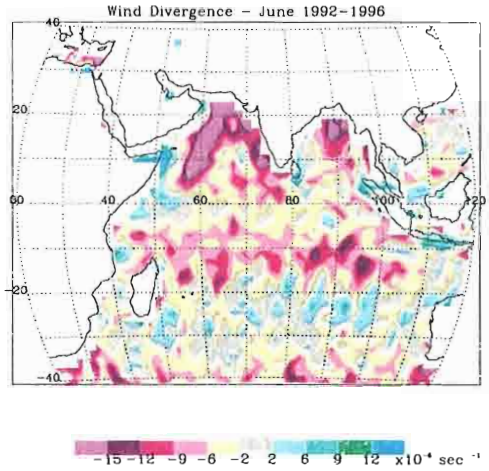


(a) June

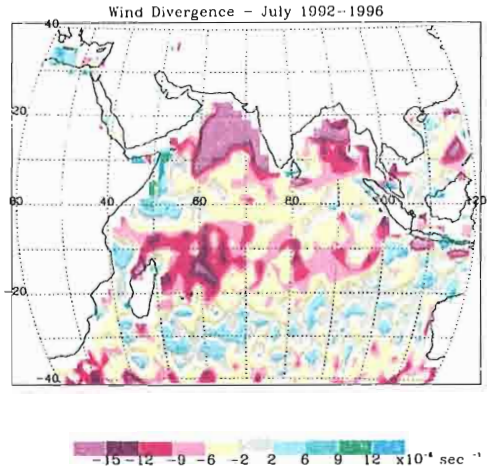


(b) July

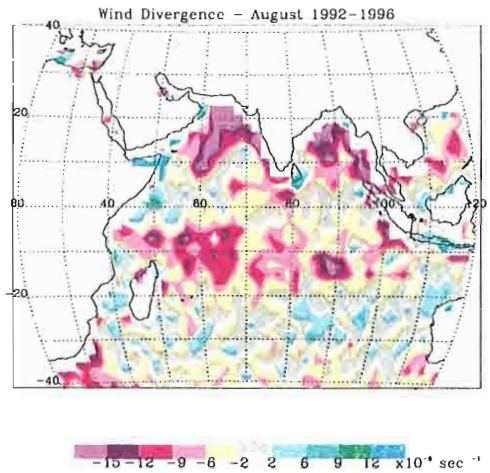


(c) August

Figure 6: Same as figure 4 except for June, July, and August.

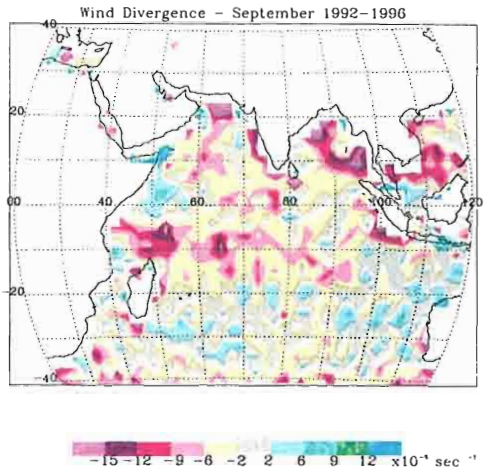


(a) September

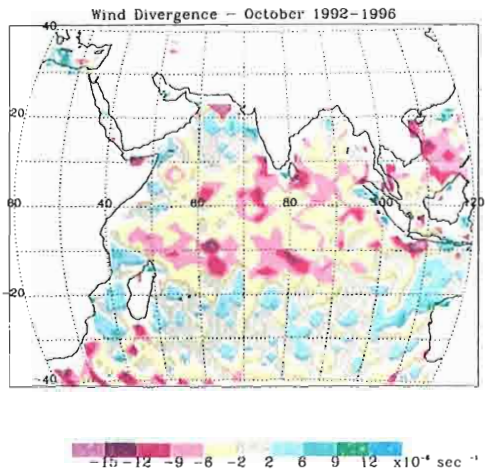


(b) October

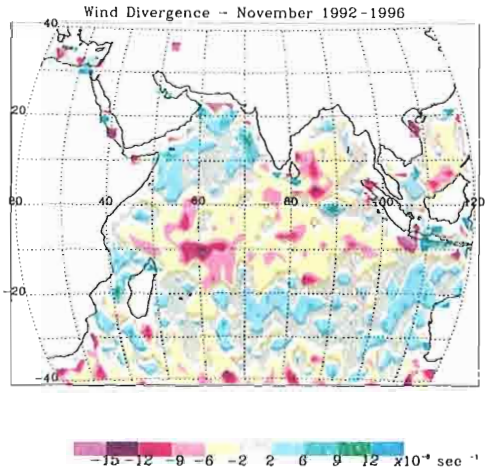


(c) November

Figure 7: Same as figure 4 except for September, October, and November.

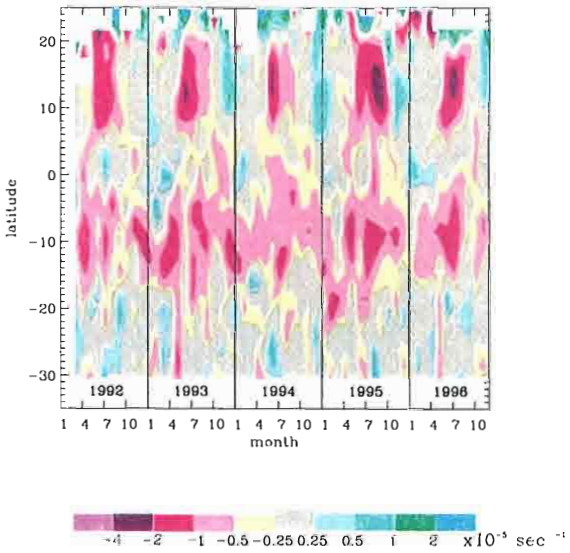


(a) Western Indian Ocean (60° E).

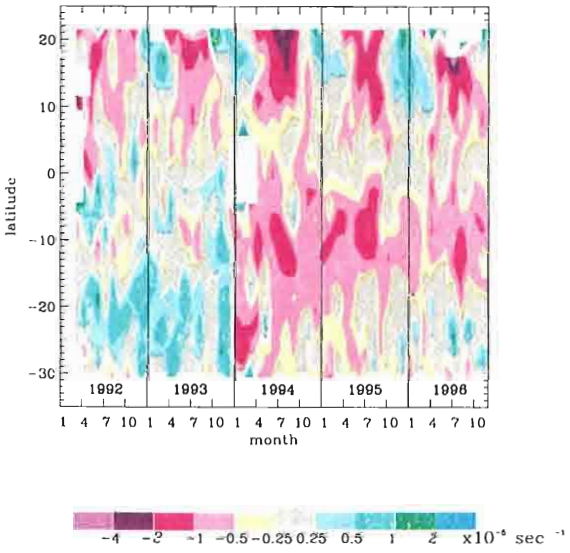


(b) Eastern Indian Ocean (90° E).

Figure 8: Variations in divergence in the (a) eastern Indian Ocean (60° E) and (b) western Indian Ocean (90° E). White spaces indicate areas of missing divergence data. Convergence is shown as negative divergence. Units of divergence are $10^{-5}$ $s^{-1}$.

Convergence is shown as negative divergence. Units of divergence are $10^{-5}$ $s^{-1}$.

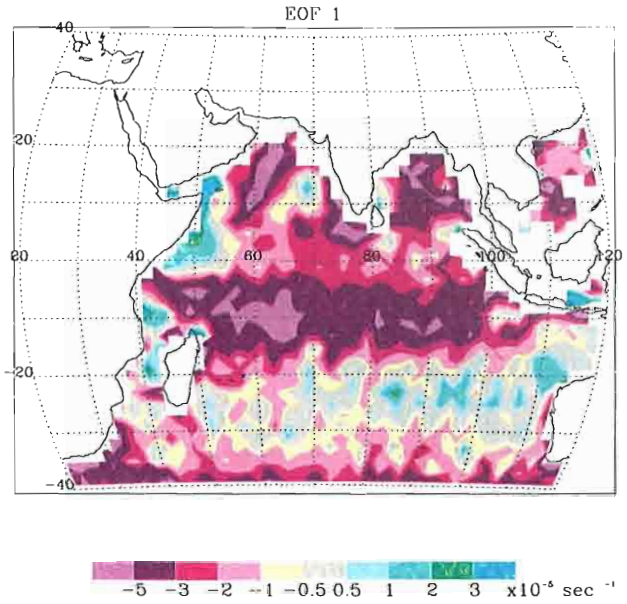


(a) Spatial component of the first EOF

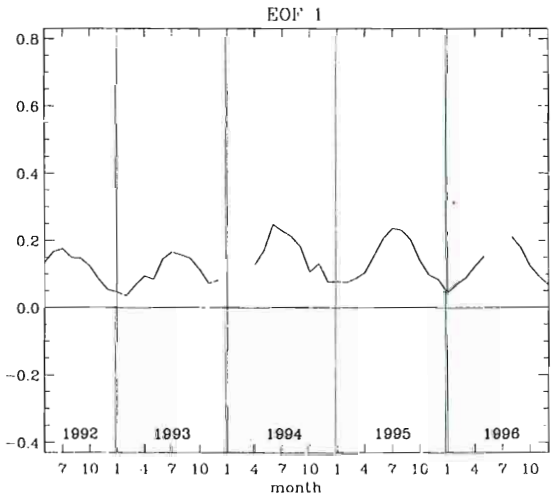


(b) Temporal component of the first EOF

Figure 9: The first Empirical Orthogonal Function (EOF). Gaps in the time series indicate months excluded from the analysis. Units of the spatial function are $10^{-5}$ $s^{-1}$.

indicate months excluded from the analysis. Units of the spatial function are $10^{-5}$ $s^{-1}$.

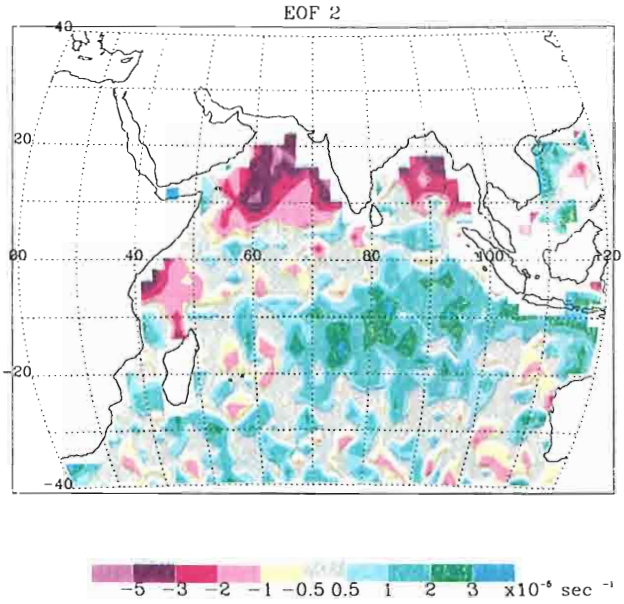


(a) Spatial component of the second EOF

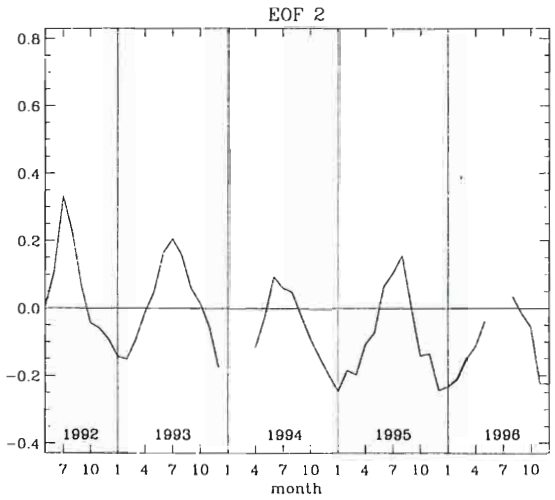


(b) Temporal component of the second EOF

Figure 10: Same as Figure 9 except for the second EOF.

Figure 10: Same as Figure 9 except for the second EOF.

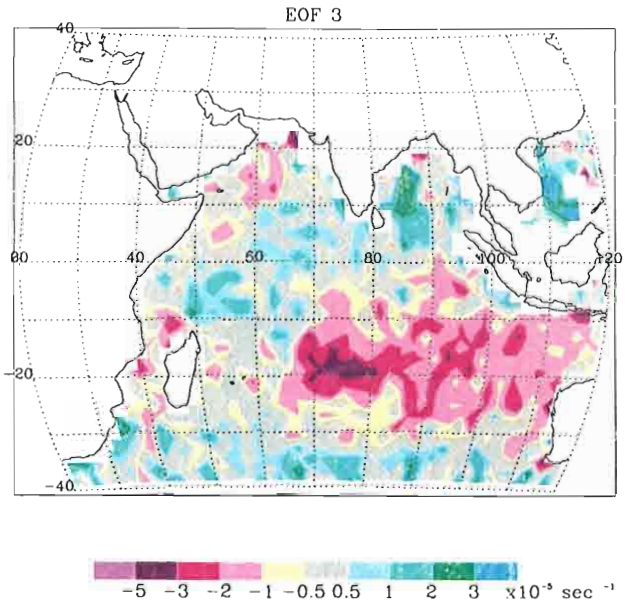


(a) Spatial component of the third EOF

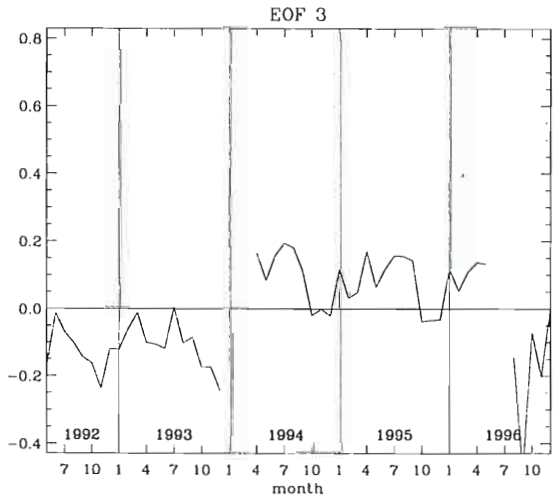


(b) Temporal component of the third EOF

Figure 11: Same as Figure 9 except for the third EOF.

Figure 11: Same as Figure 9 except for the third EOF.

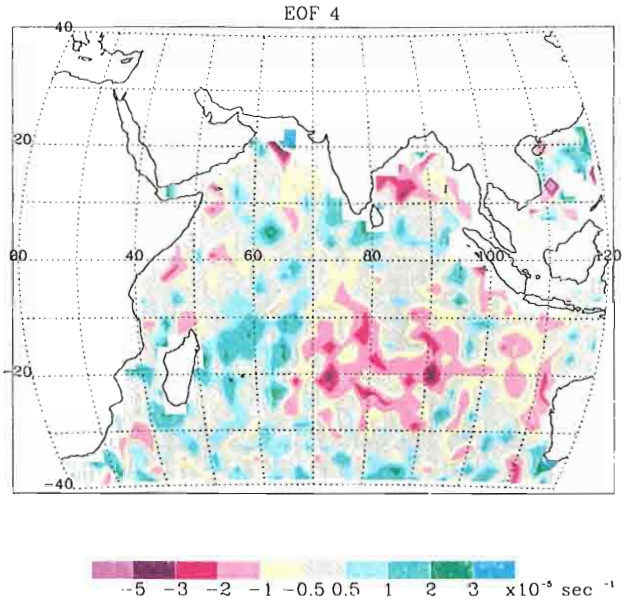


(a) Spatial component of the fourth EOF

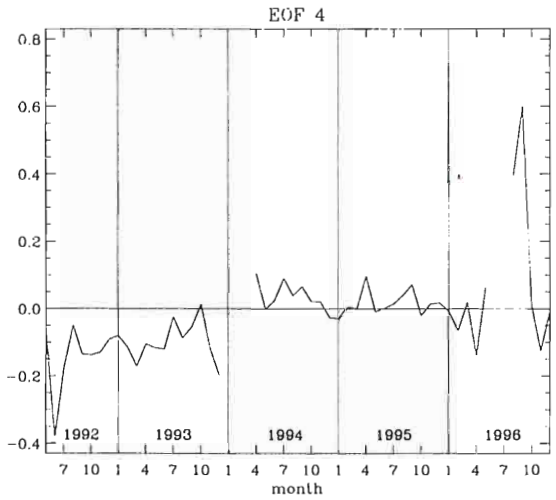


(b) Temporal component of the fourth EOF

Figure 12: Same as Figure 9 except for the fourth EOF.

Figure 12: Same as Figure 9 except for the fourth EOF.

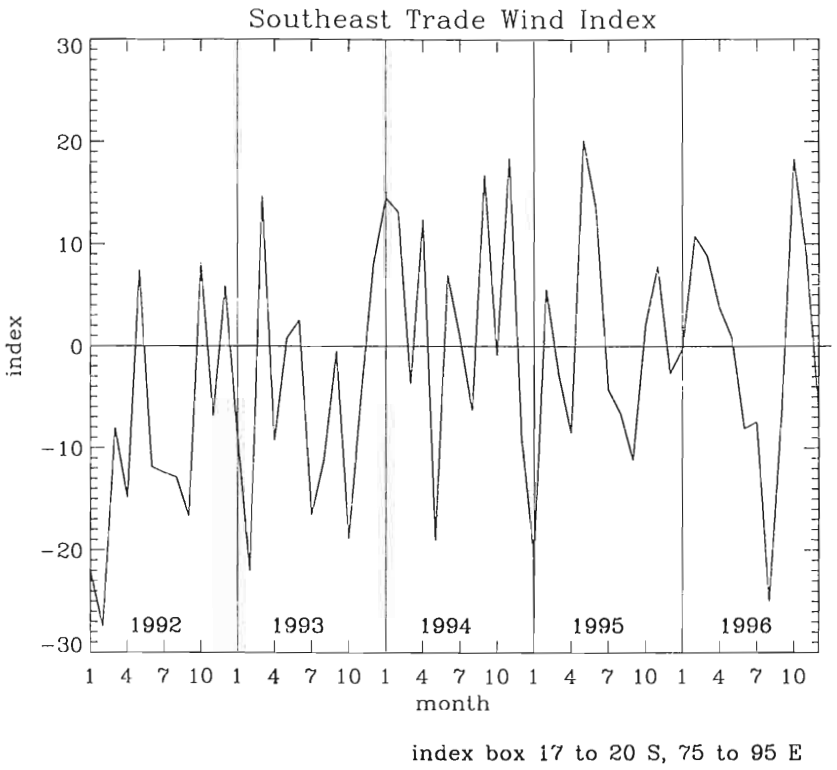


Figure 13: Southeast Indian Ocean Trade Wind Index. This index shows the average deviation from monthly climatology of winds in a box stretching from 75° E to 95° E and 16° S to 20° S. Units are $ms^{-1}$.

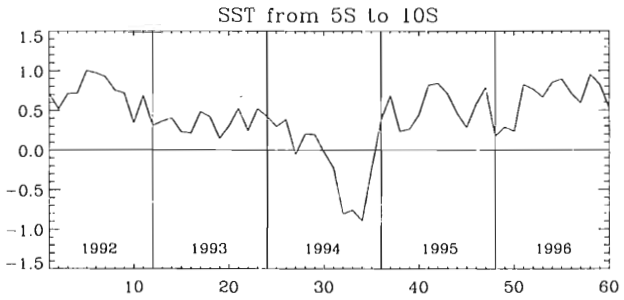


(a) SST.

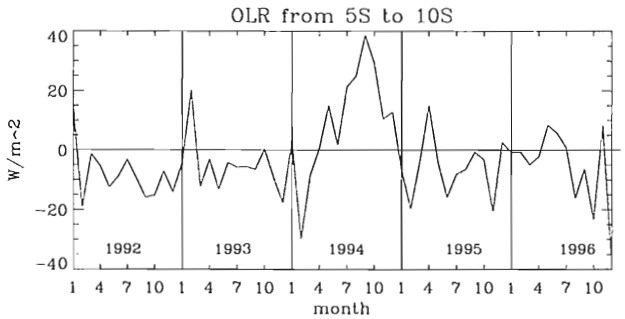


(b) OLR.

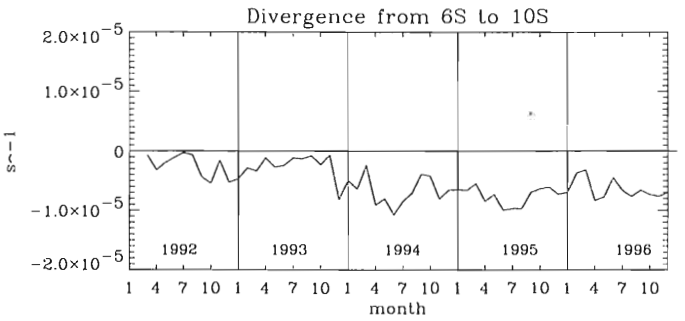


(c) Divergence.

Figure 14: SST, OLR, and divergence 5° S (6° S for divergence) to 10° S. (a) Reynolds SST anomalies averaged over a box extending from 80° E to 105° E. Units are °C. (b) CAC OLR anomalies averaged over 80° E to 105° E. Units are $Wm^{-2}$. (c) Divergence averaged over 80° E to 106° E. Units are $s^{-1}$.

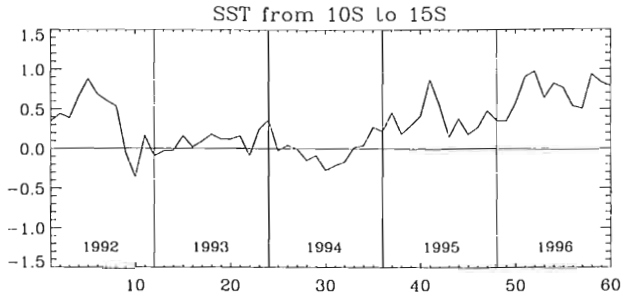


(a) SST.

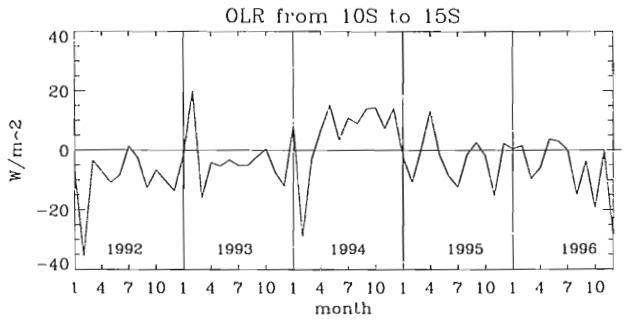


(b) OLR.

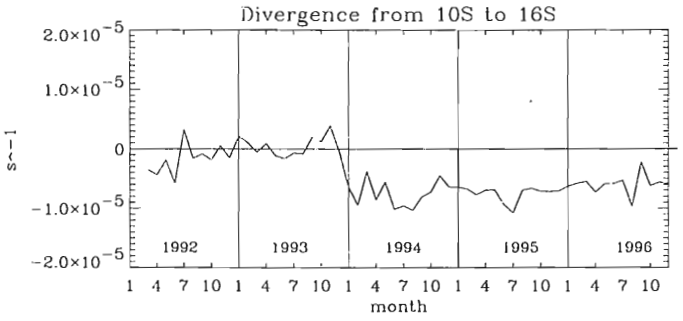


(c) Divergence.

Figure 15: SST, OLR, and divergence 10° S to 15° S (16° S for divergence). (a) Reynolds SST anomalies averaged over a box extending from 80° E to 105° E. Units are °C. (b) CAC OLR anomalies averaged over 80° E to 105° E. Units are $Wm^{-2}$. (c) Divergence averaged over 80° E to 106° E. Units are $s^{-1}$.

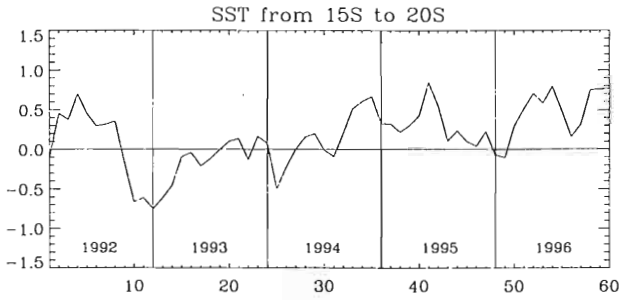


(a) SST.

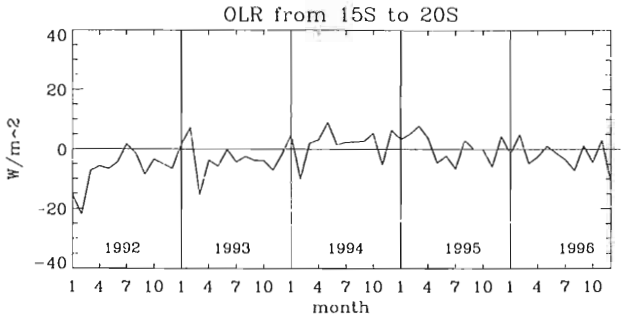


(b) OLR.

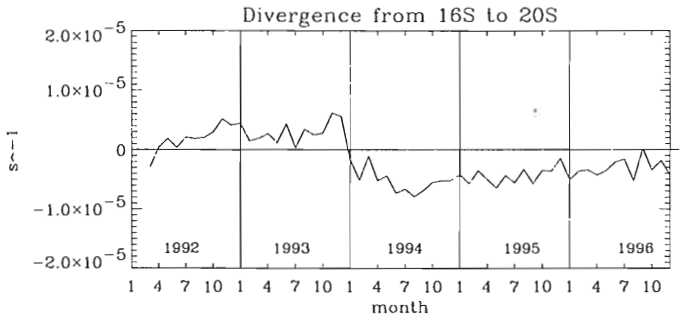


(c) Divergence.

Figure 16: SST, OLR, and divergence 15° S (16° S for divergence) to 20° S. (a) Reynolds SST anomalies averaged over a box extending from 80° E to 105° E. Units are °C. (b) CAC OLR anomalies averaged over 80° E to 105° E. Units are $Wm^{-2}$. (c) Divergence averaged over 80° E to 106° E. Units are $s^{-1}$.

# 5. SUMMARY AND CONCLUSIONS

We use the divergence theorem as the basis for calculating surface wind divergence from ERS-1 and ERS-2 10 m scatterometer winds. This method is better for satellite data, since it involves no averaging over time or space prior to calculations. It is also easier to implement on swath data because of the lack of sensitivity to missing cells. After performing the calculations on five years of data from January 1992 to December 1996, we find both seasonal and interannual variations within the resulting divergence data.

The seasonal cycle associated with the Asian monsoon flow over the Arabian Sea and Bay of Bengal is the most dominant feature over the northern Indian Ocean. Strong convergence accompanies the onset of the monsoon during May and continues through August. The northern winter months are characterized by divergence in this region.

The ITCZ over the southern Indian Ocean has both a seasonal and an interannual component to its variability. Seasonally, the ITCZ experiences changes in strength and location. The western portion of the region is farthest south (north) during northern winter (summer). It is relatively strong at either extreme; it weakens during the transition periods.

Over the central and eastern Indian Ocean, the ITCZ stays in approximately the same location; however, it is strongest during southern summer and weakest in southern winter. The southeastern Indian Ocean also has a distinct interannual component. A general strengthening of the southeast trade winds in 1994 may cause in southern winter. The southeastern Indian Ocean also has a distinct interannual component. A general strengthening of the southeast trade winds in 1994 may cause

a change in the nature of the divergence in this region. The ITCZ is stronger and larger for the latter part of the period, and a divergence zone near 20° S disappears.

The change in divergence in 1994 may be explained by strenghthened trade winds over the southeast Indian Ocean. Evidence of the change in divergence patterns can be detected in the SST and OLR patterns, resulting in increasing SST and decreasing OLR.

This interannual component, as well as some of the seasonal features, have not been previously noted in other studies of the Indian Ocean atmospheric circulation. The increased coverage and resolution of scatterometer provides a more complete view of the circulation over the global oceans, allowing for a better overall description of wind and, when using our method, surface wind divergence features.

# REFERENCES


Bourassa, M. A., M. H. Freilich, D. M. Legler, W. T. Liu, and J. J. O'Brien, Wind observations from new satellite and research vessels agree, *EOS Trans.*, *78*, 597–602, 1997.

Ebuchi, N., and H. C. Graber, Directivity of wind vectors derived from the ERS-1/AMI scatterometer, *J. Geophys. Res.*, *103*, 7787–7797, 1998.

Halpern, D., M. H. Freilich, and R. S. Dunbar, ERS-1 scatterometer estimates of annual variations of Atlantic ITCZ and Pacific NECC, *ESA SP*, *361*, 1003–1008, 1994*a*.

Halpern, D., V. Zlotnicki, O.Brown, M. Freilich, and F. Wentz, An atlas of monthly mean distribution of SSMI surface wind speed, ARGOS buoy drift, AVHRR/2 sea surface temperature, AMI surface wind velocity, and ECMWF surface wind components during 1992, JPL Publication 94-4, Jet Propulsion Laboratory, Pasadena, 143 pp., 1994*b*.

Halpern, D., M. H. Freilich, and R. A. Weller, Arabian sea surface winds and ocean transports determined from ERS-1 scatterometer, *J. Geophys. Res.*, *103*, 7799–7805, 1998.

Hastenrath, S., *Climate dynamics of the tropics*, Kluwer Academic Publishers, Boston, 488 pp., 1991.

Hastenrath, S., and P. J. Lamb, On the dynamics and climatology of surface flow over the equatorial oceans, *Tellus*, *30*, 436–448, 1978.

Holton, J. R., *An introduction to dynamic meteorology*, Academic Press, New York, 3rd edition, 511 pp., 1992.

Hsu, C. S., W. T. Liu, and M. G. Wurtele, Impact of scatterometer winds on hydrologic forcing and convective heating through surface divergence, *Mon. Wea. Rev.*, *125*, 1556–1576, 1997.

Jury, M. R., and B. Pathack, A study of climate and weather variability over the tropical southwest Indian Ocean, *Meterol. Atmos. Phys.*, *47*, 37–48, 1991.

Jury, M. R., B. Pathack, and D. E. Waliser, Evolution and variability of the ITCZ in the southwest Indian Ocean, *Theor. Appl. Climat.*, *48*, 187–294, 1994.

Legler, D. M., Empirical orthogonal function analysis of wind vectors over the tropical [illegible], and D. E. Waliser, Evolution and variability of the ITCZ in the southwest Indian Ocean, *Theor. Appl. Climat.*, *48*, 187–294, 1994.

Legler, D. M., Empirical orthogonal function analysis of wind vectors over the tropical Pacific region, *Bull. Amer. Meteor. Soc.*, *64*, 234–241, 1983.

Legler, D. M., J. N. Stricherz, and J. J. O'Brien, TOGA pseudo-stress atlas 1985-1994: III Indian Ocean, technical report 97-3, COAPS/Florida State University, Tallahassee, FL, 163 pp., 1997.

Meyers, G., Variation of the Indonesian throughflow and the El Niño- Southern Oscillation, *J. Geophys. Res.*, *101*, 12255–12263, 1996.

J. J. O'Brien (Ed.), *Scientific opportunities using satellite wind stress measurements over the ocean: Report of the Satellite Surface Stress Working Group*, Nova University/N.Y.I.T. Press, Fort Lauderdale, 1982.

Philander, S. G. H., *El Niño, La Niña, and the Southern Oscillation*, Academic Press, New York, 1st edition, 263 pp., 1990.

Quilfen, Y., *WNF ERS off-line wind scatterometer products – users manual*, Cent. ERS d'Arch. et de Trait., rep. C2-MUT-W-01-IF, 1996.

Reason, C. J. C., R. J. Allen, and J. A. Lindesay, Evidence for the influence of remote forcing on interdecadal variability in the southern Indian Ocean, *J. Geophys. Res.*, *101*, 11867–11882, 1996.

Reynolds, R. W., and T. M. Smith, Improved global sea surface temperature analyses using optimum interpolation, *J. Climate*, *8*, 1571–1583, 1994.

Stricherz, J. N., D. M. Legler, and J. J. O'Brien, Atlas of Florida State University Indian Ocean winds for TOGA 1970-1985, technical report, COAPS/Florida State University, Tallahassee, FL, 216 pp., 1993.

Waliser, D. E., and C. Gautier, A satellite derived climatology of the ITCZ, *J. Climate*, *6*, 2162–2174, 1993.

Wilks, D. S., *Statistical methods in the atmospheric sciences*, Academic Press, New York, 464 pp., 1995.

Zheng, Q., X.-H. Yan, W. T. Liu, W. Tang, and D. Kurz, Seasonal and interannual variability of atmospheric convergence zones in the tropical Pacific observed with ERS-1 scatterometer, *Geophys. Res. Let.*, *24*, 261–263, 1997.

Zheng, Q., X.-H. Yan, W. T. Liu, W. Tang, and A. H. Ali, Global tropical ocean atmospheric convergence zones derived from ERS-1/2 and NSCAT scatterometer winds, *Ninth Conf. on Interaction of the Sea and Atmosphere*, 40–43, 1998.

# BIOGRAPHICAL SKETCH

## Degrees

B.S. in Meteorology 1996, The Pennsylvania State University.

Minor in Mathematics 1996, The Pennsylvania State University.

M.S. in Meteorology anticipated Summer 1998, Florida State University.

## Experience

Center for Ocean-Atmospheric Prediction Studies, Florida State University, Tallahassee, FL. Graduate Student Researcher. Investigated the variations in tropical convergence zones using surface wind data from scatterometers mounted on satellites. Developed the computer code necessary to complete all the necessary calculations. Created graphics and animations for presentations and publications. Major professor: Dr. James J. O'Brien.

PRC, Inc., McLean, VA; 1995. Intern. Assisted with the database design of the Advanced Weather Interactive Processing System (AWIPS) project.

Accu-Weather, Inc., State College, PA; 1994. Forecasting Intern.

Capital Broadcasting Company/WRAL-TV5, Raleigh, NC; 1993. Weather Center Intern.

Campus Weather Service, The Pennsylvania State University, University Park, PA; 1992-1996. Shift Manager. Led student forecasters in preparation and dissemination of forecasts to local radio stations.

1992-1996. Shift Manager. Led student forecasters in preparation and dissemination of forecasts to local radio stations.

## Computer experience

Developed FORTRAN and C code to perform calculations on satellite scatterometer data. Utilized IDL for development of graphics and animations, as well as statistical calculations involving scalar and vector data. Studied the Fifth Generation Penn State/NCAR Mesoscale Meteorology Model (MM5) and the associated adjoint model. Utilized GEMPAK and McIdas for displaying meteorological data.

Experienced with MS Word, WordPerfect, LaTeX , MS Excel, HTML, and MS PowerPoint.

Familiar with UNIX, Mac (System 7.5.3), PC (Windows 3.x, 95, and NT), and VAX/VMS platforms.

## Honors

American Meteorological Society/Industry Undergraduate Scholarship Recipient, 1994-1996.

Phi Kappa Phi National Honor Society, inducted 1996

High Distinction and Honors Graduate, The Pennsylvania State University, 1996.

## Memberships

American Geophysical Union

Chi Epsilon Pi Meteorology Society